Steering Cu-based CO_2RR Electrocatalysts Selectivity: the Effect of Hydroxyapatite Acid/Base Moieties in promoting Formate Production

M. Ferri [a], L. Delafontaine* [b], S. Guo [b], T. Asset [b], P. Cristiani [c], S. Campisi [a], A. Gervasini [a], P. Atanassov [b]*

[a] Università degli Studi di Milano, Dipartimento di Chimica, Via Golgi 19, Milan, Italy

[b] University of California Irvine, Department of Chemical and Biomolecular Engineering, Irvine, USA

[c] RSE, Ricerca sul Sistema Energetico, Milan, Italy

** These authors contributed equally to the paper*

Abstract

Among all CO_2 reduction reaction (CO_2RR) active metals, copper is the only one which exhibits optimal *CO binding energy for multiple electron transfers. Despite such a unique feature, the use of Cu-based CO_2RR catalysts at the industrial scale is hampered by large overpotentials and poor selectivity. In this realm, the introduction of acid/basic functionalities at the catalyst surface may help to both overcome scaling relations (i.e. lower CO_2RR overpotential) and tune the selectivity of Cu-based catalysts. Herein, we demonstrate that an amphoteric calcium phosphate additive (Hydroxyapatite, HAP, $Ca_{10}(PO_4)_6(OH)_2$) alters the product distribution from Cu-based catalysts by steering CO_2RR selectivity towards liquid oxygenated products, promoting formate production over CO.

TOC

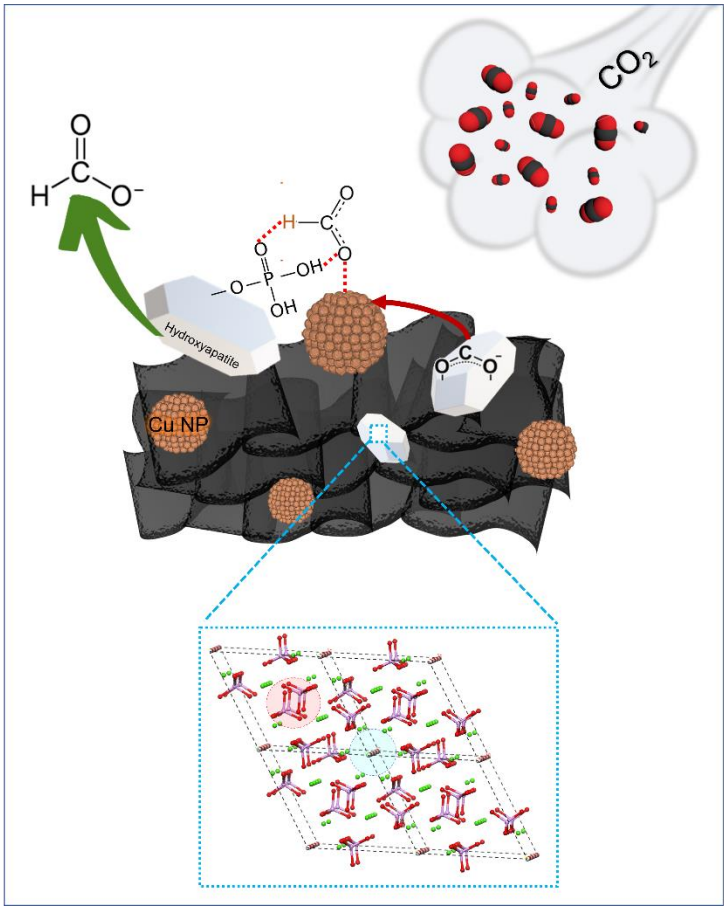

Main Text

The flourishing of the global economy and continuous population growth, driven by industrial progress, has relied on the massive utilization of fossil fuels for energy generation. Therefore, the relentless emission of carbon dioxide has risen its atmospheric concentration to *ca*. 421 ppm in 2022 (against a safety upper concentration limit of 350 ppm) [1], with consequent climate change issues and environmental repercussions. With a forecasted CO_2 concentration of *ca*. 600-700 ppm by the end of the century, carbon capture and utilization (CCU) technologies are attracting great attention from the perspective of a transition towards a more sustainable future [2].

Among CCU processes, the electrochemical CO_2 reduction reaction (CO_2RR) holds great promise for recycling CO_2 as feedstock for chemicals and fuels production while providing a means for the storage of intrinsically intermittent renewable energy sources in a power-to-fuel concept [3]. Since the pioneering discovery by Hori [4], who uncovered metals ability to convert CO_2 under cathodic potential in aqueous systems, several materials have been developed and tested as CO_2RR electrocatalysts, aiming to improve the energetics (i.e. cell potential E_{cell}), kinetics (i.e. current density *i*) and selectivity (i.e. faradaic efficiency, FE) of the process.

Although major progresses have been made and industrial scale CO_2 electrolyzers are seeing light [5], CO_2RR still suffers from several problems such as (*i*) poor selectivity, (*ii*) limited energy efficiencies, (*iii*) sluggish kinetics, (*iv*) mass transport limitations, (*v*) challenging product separation and (*vi*) catalyst stability/durability [3]. If issues from *(iv)* to *(vi)* may be fixed by the proper engineering of electrodes and electrolyzers (i.e. gas diffusion electrode fabrication [6,7] and implementation of flow-cells [8]), issues from *(i)* to *(iii)* are intrinsically related to the catalytic system.

Copper is undisputedly the most studied metal in CO_2RR as it is the only element able to drive the reduction to C_1 or C_{2+} hydrocarbons and/or oxygenates [9]. Such peculiar behavior stems from Cu optimal binding energy with *CO, the key intermediate in the generation of all reaction products requiring > 2 electron transfers (i.e. more reduced than HCOOH and CO) [10]. Despite such ideal intermediate binding energy, Cu-based catalysts exhibit poor selectivity and large overpotentials. This selectivity problem is exacerbated towards C_{2+} products because of the presence of common intermediates leading to a multitude of products [9] and linear scaling relationships between relevant binding energies[10]. In particular, linear scaling relationships disallow altering independently the binding energy of a single intermediate to favor CO_2RR to a desired product, therefore impeding to obtain more reduced products (i.e. alcohols and hydrocarbons) at small overpotential.

Nonetheless, several parameters such as nanoparticle size [11] and shape [12] and thermal/synthetic history [13] of Cu-based catalysts have been investigated, always aiming to enhance the efficiency of the process and/or tune CO_2RR selectivity. Furthermore, active phase/support interaction have been exploited to boost Cu nanoparticle activity and selectivity towards specific products while improving conductivity and preventing aggregation of the same nanoparticles. For example, Collins et al. reported that 25 nm Cu nanoparticles were significantly more selective towards C_2H_4 when supported on single-wall carbon nanotubes compared to electrodeposited Cu films (FE ≈ 41% vs. ≈ 19%, E = -2.2 V vs Ag/AgCl) [14]. Similarly, Sun et al. observed major increases in FE_{C2H4} when supporting 7 nm Cu nanoparticles onto N-doped graphene instead of carbon black (*ca*. 79% vs 6.3%, E = -1.1 V vs RHE) [15], while an outstanding performance was delivered by Cu nanoparticles on N-doped carbon nanospikes, reaching a remarkable FE ≈ 63% towards ethanol at -1.2 V vs RHE [16]. Both authors attributed such improved selectivity towards

C_{2+} products to the presence of N moieties in the support: besides tightly anchoring Cu nanoparticles, these sites (Lewis bases) may behave as reservoir of $CO_{2(ads)}$ and *H species, facilitating the overall process.

It is interesting to note that, despite the evidence that acid/base functional groups may influence catalyst CO_2RR selectivity by acting on surface stabilization of intermediates, the use of acid/basic additives has rarely been investigated in this field. Recently, Xu et al. [17] reported that the presence of phosphate groups on the surface of electrodeposited Cu electrodes increases $HCOO^-$ faradaic efficiency by a factor *ca*. 2.5 as compared to Cu foil.

Hydroxyapatite (HAP, $Ca_{10}(PO_4)_6(OH)_2$) is a calcium phosphate characterized by marked water insolubility ($K_{ps} \approx 4.7 \cdot 10^{-59}$, [18]), thermal and chemical stability and peculiar surface properties. Indeed, HAP possesses a highly functionalized and amphoteric surface [19,20], which in turn results in a particular affinity towards CO_2 [21,22]. CO_2 (and eventually CO_2RR intermediates) may indeed be stabilized onto HAP acid and/or basic sites, coordinating to the surface accordingly [20]. Such coordinative ability of HAP is critical for directing the reaction pathway and determining the selectivity in CO_2 reduction reaction, as recently pointed out by Wai et al., who studied carbon dioxide methanation over nickel hydroxyapatite catalysts [23]. In particular, *in situ* DRIFTS measurements at different temperatures proved that surface hydroxyl (*OH) and oxide (*O) groups from HAP phosphates are directly involved in the interaction with chemisorbed CO_2 to form hydrogen-carbonates (HCO_3*), which then undergo further hydrogenation to be transformed into bidentate formate specie (HCOO*).

Additionally, HAP Brønsted acid sites (PO-H) could act as proton donors/acceptors, facilitating the proton transfers required by the reaction. To date, no application of HAP in electrocatalytic CO_2RR has been reported, although a few papers have implemented it in catalytic [23] and photocatalytic [24,25] applications.

With the purpose of studying the effect introduced by acid/basic HAP functionalities on CO_2RR selectivity, we first designed and synthesized a catalyst composed by Cu nanoparticles (25 nm in size) supported onto a 3D assembly of N-doped graphene nanosheets (3D-GNS, [26,27]). Secondly, admixing with HAP has been performed and the differences in electrocatalytic performance analyzed.

The Cu-based and Cu-based HAP-admixed catalysts, hereinafter referred to as Cu/3D-GNS and Cu+HAP/3D-GNS respectively, has been synthesized starting from the individual materials and following a stepwise procedure aimed to guarantee the maximum dispersion of both Cu and HAP nanoparticles (NPs) onto 3D-GNS. Obtained electrocatalysts exhibited 20 wt.% Cu and 10 wt.% HAP loading by design (molar Cu to HAP ratio equal to *ca*. 30). The detailed synthetic route can be found in the Supporting Information.

The pristine support (3D-GNS) and both catalysts have been structurally and morphologically characterized by means of N_2 adsorption/desorption isotherms, STEM/EDX and XPS. Figure 1 reports the main outcomes of Cu+HAP/3D-GNS characterization while additional data are available in the Supporting Information (Figures S1 to S4 and Table 1), together with the experimental and instrumental details.

Overall, the structural and morphological features of the support are retained upon both immobilization of the active phase (Cu NPs) and of the additive (HAP). All samples exhibit type IV N_2 ads/des isotherms with H2 type hysteresis loop (Figure 1a and Figure S1), which identifies them as strictly mesoporous materials, as further confirmed by their pore size distribution (Figure S1). However, a decrease in both surface area (SA) and pore volume (V_{Pore}) is registered upon Cu NPs immobilization (Table

1), possibly caused by a partial pore obstruction by Cu NPs, which size matches that exhibited by 3D-GNS pores (Figure S1 and reference [26]).

STEM images (Figure 1b, Figure S2) confirm that the three-dimensional open pore structure of 3D-GNS is preserved in both catalysts, guaranteeing optimal mass diffusion of reactants and products under reaction conditions.

Focusing on the Cu/3D-GNS catalyst (Figure S2), STEM images display both large Cu aggregates and small, finely dispersed Cu NPs. If the presence of large deposits may be ascribed to partial aggregation, the detection of Cu NPs with size < 25 nm may be due to a poor distribution of the commercial nanoparticles themselves. The successful admixing with HAP in Cu+HAP/3D-GNS samples is confirmed by the observation of HAP platelets all over the surface of the support (Figure S2), although for STEM images it is impossible to assess their close contact with Cu NPs. However, EDX maps display an effective overlap between Ca and P (i.e. HAP) and Cu signals (Figure 2c), thus indicating that a cooperation between the active phase and the acid/basic moieties of HAP may be expected.

XPS surveys of both pristine support and catalysts (Figure S3) provided an overview of the functional groups and surface atomic concentration at the surface; the related quantitative elemental analysis results are reported in Table 1. Each sample displays the typical contributions of its constitutive elements, namely carbon (C 1s, *ca*. 285 eV), oxygen (O 1s, *ca*. 533 eV) and nitrogen (N 1s, *ca*. 400 eV) for pristine 3D-GNS; additional copper (Cu $2p_{3/2}$, *ca*. 930 and Cu $2p_{1/2}$, *ca*. 960 eV) for Cu/3D-GNS; additional calcium (Ca 2p, *ca*. 350 eV and Ca 2s, *ca*. 440 eV) and phosphorus (P 2p at *ca*. 140 eV and P 2s at *ca*. 195 eV) for Cu+HAP/3D-GNS. Interestingly, at.% of Ca and P in Cu+HAP/3D-GNS are adherent to the effective HAP wt.% loading and their atomic ratio (*ca*. 1.62 against the stoichiometric 1.67) confirms no other calcium phosphate phases were formed upon admixing.

Quantitative results obtained for pristine 3D-GNS are consistent with literature [28]. Likewise, deconvolution of high-resolution XPS spectra of C 1s and N 1s (Figure S4) revealed the predominant graphitic (sp^2 C, *ca*. 36% of total C) and pyridinic (*ca*. 31% of total N) nature of 3D-GNS structure and structural moieties, respectively (Table S1).

Regarding the Cu surface atomic concentration, the values detected in Cu/3D-GNS and Cu+HAP/3D-GNS (Table 1) are *ca*. 10 times lower than expected by design. Possible explanations of such results could be: (*i*) the combination of 3D-GNS extended porous structure and moderate Cu loading, which may lead to the confinement of Cu NPs in the pores of the support; (*ii*) Cu NP partial aggregation and/or inhomogeneous dispersion; (*iii*) the fact that XPS, as a surface technique, yields an at.% quantification which may not be relatable to the volume ratio of the sample constitutive elements, especially for composite materials. The analysis of the Cu $2p_{3/2}$ region for both Cu/3D-GNS and Cu+HAP/3D-GNS (Figure 1d) revealed the presence of modest amount of Cu species in low oxidation states (metallic copper or Cu(I), at 932.5 eV, Table S2). In any case, the HR spectra were dominated by the peaks related to Cu(II) species, namely CuO (933.8 eV, Table S2), $Cu(OH)_2$ (935.1 eV, Table S2) and the related Cu(II) shake peaks (942-948 eV, Table S2). An additional component in the region between 936-938 eV was present exclusively in Cu+HAP/3D-GNS sample. This component might be ascribed to electron-poor Cu(II) species surrounded by electronegative groups, that in this specific case might be associated with hydroxyl and phosphate surface groups of HAP.

After characterization, inks were made out of catalyst powders and gas diffusion electrodes (GDEs) were fabricated by drop-casting. Such GDEs have been tested as cathodes in a lab-scale

microfluidic CO_2 electrolyzer (i.e. electrochemical flow-cell, Figure S5). All the experimental details, from GDEs fabrication to electrochemical testing and products analyses, are available in the Supporting Information.

Nyquist plots (Figure 2a) reveal a low uncompensated resistance of the cell. For both Cu/3D-GNS and Cu+HAP/3D-GNS GDEs, a similar R_{ct} indicates that the presence of HAP, a ceramic and thus insulating compound, does not impact on the electron transfer ability of the catalytic system.

Linear scan voltammetry (LSV) curves of both catalyst have been collected feeding the cell either with N_2 (0.1 M PBS) or CO_2 (0.175 M $KHCO_3$) (Figure 2b) as to evaluate the magnitude of CO_2RR versus HER competition on the catalysts. For both Cu/3D-GNS and Cu+HAP/3D-GNS samples, a net increase of the current densities delivered at potentials lower than -0.6 V vs RHE is observed when switching from N_2 to CO_2 feeding. This confirms that, despite the unavoidable presence of parasitic HER, the catalysts exhibit CO_2RR activity. Admixing with HAP results in a slightly increase of the delivered current densities under both N_2 and CO_2 feeding. Such result suggests that HAP basic moieties (i.e. surface hydroxyl *OH and oxide *O groups from phosphates [20]) might be able to foster both HER and CO_2RR, acting as a reservoir/supplier of protons or CO_2 molecules to the vicinal Cu NPs. However, as the ratio of the current densities delivered under different gas feeding is similar for both catalysts, HAP does not suppress and/or enhance neither HER nor CO_2RR. From these considerations, only an effect on the CO_2RR product distribution may be envisage by HAP admixing.

As to shed light on the product distribution yielded by the catalysts, 30 minutes long chronoamperometric (CA) test, coupled with ex-situ determination and quantification of the reaction products, have been carried out (sample GC traces and ^{1}H-NMR spectra available in the Supporting Information, Figure S6 and S7). The product distribution of Cu/3D-GNS and Cu+HAP/3D-GNS is reported in Figure 2c while numerical data are available in the Supporting Information (Table S3).

The relative HER and CO_2RR faradaic efficiencies, plotted in Figure S8, are consistent with the LSV data, showing a predominance of HER at potentials less cathodic than -1.0 V vs RHE. Moving towards more cathodic potentials (more negative than -1.0 V vs RHE), a *ca*. 50% FE_{CO2RR} is reached by both catalysts, with slightly higher values for Cu+HAP/3D-GNS. Going into the details of CO_2RR selectivity, the main product for both catalysts is formate (Figure 2c), followed by CO and traces of methane and ethylene (Figure S9). Focusing at first on the Cu/3D-GNS product distribution, the low FE in ethylene, normally detected in higher amounts on large size Cu^0 NPs, might be related to the use of 0.5 M $KHCO_3$ as electrolyte. Indeed, the CO* coupling that leads to the ethylene production pathway is favored under strongly alkaline conditions [29]. The buffering ability of concentrated $KHCO_3$, together with the moderate current densities achieved during the test (limiting the alkalinization at the catalyst/electrolyte interphase [30]), probably concur in steering the CO_2RR process selectivity towards C_1 products. On the other hand, the predominance of formate on CO and methane could be ascribed to the preferential stabilization of formate intermediates by the 3D-GNS moieties of the support [31].

Admixing with HAP does not alter significantly the competition between CO_2RR and the parasitic HER (Figure 2c, Figure S8 and S10), as expected from LSVs. Despite at a first sight the admixing with HAP seems not to alter the product distribution either, calculating the ratio of formate to CO faradaic efficiencies unravels the effect of HAP itself on the CO_2RR reaction pathways (Figure 2d). Indeed, net of the same trend versus applied potential, the formate to CO FE ratio of Cu+HAP/3D-GNS is shifted to higher values, indicating HAP is able to steer the selectivity towards formate (Figure 2d). This observation is in

agreement with what observed by Xu et al. [17] and Wai et al. [23], respectively for the electrochemical CO_2RR on phosphate decorated Cu electrodes and the carbon dioxide methanation over nickel hydroxyapatite catalysts.

Running longer CA tests (up to 120 minutes) and monitoring the product distribution over time shows that both catalysts exhibit stable performance and invariant selectivity as well (Figure S11). Noticeably, throughout the whole extended reaction time, the formate to CO FE ratio remains higher for the HAP admixed catalyst (Figure S12). It is worth noting that XPS characterization of used catalysts confirmed the stability of these systems, whose surface Cu content was almost the same (at.% ca. 0.3 %) before and after testing. The decomposition of HR spectra revealed just slight differences in the relative distribution of copper species with an increase of Cu(0) and Cu(I) compared to Cu(II) observed for the HAP admixed catalyst in the post-electrolysis sample. Although usually used for samples with a lower proportion of Cu(II), the Cu LMM peak may be used to qualitatively assess the ratio of Cu(0) to Cu(I) with the Cu/3D-GNS sample showing primarily Cu(0) and the Cu+HAP/3D-GNS sample showing a mixed proportion of Cu(0) and Cu(I) species (Table S2 Figure S13 and S14).

A tentative mechanism of CO_2 reduction on Cu+HAP/3D-GNS is proposed in Figure 3. Based on the few reports available in literature about the effect of phosphate groups on CO_2 reduction mechanisms [23], it might be presumed that phosphate groups themselves promote the formation of a H_{ads} species, supplying a proton to Cu NPs upon the first electron transfer. Then, this H_{ads} might follow the typical parasitic HER route to form H_2 or favor the formation of a $HCOO_{ads}$ species, resulting in the formation of a formate ion upon the second electron transfer. Although the suppression of CO production in the presence of HAP could be explained by this tentative mechanism, other effects of HAP acid/basic moieties (e.g. preferential stabilization of formate intermediates through acid-base interactions between oxygen atoms and Ca^{2+} acidic sites) on the CO_2RR pathway cannot be ruled out.

Overall, the present study indicates that the admixing of Cu-based catalysts with acid/basic additives may be a powerful strategy to bypass linear scaling relationships, which critically impact on catalysts selectivity, hampering their industrial implementation. Acid/basic moieties may indeed help in steering the CO_2RR selectivity towards specific products (in this case, formate) by means of the preferential stabilization of defined reaction intermediates. Further studies, from DFT simulations to in-situ spectroelectrochemical studies, will be aimed at disclosing the CO_2 to formate reaction pathway onto HAP admixed catalysts. With the present communication, the authors hope to stimulate further research on the effect of different acid/base (and oxo- and/or carbophilic) surface groups on CO_2RR catalysts' product selectivity, possibly paving the way to more efficient and selective electrocatalysts.

List of abbreviations

In order to guide the reader, some of the less common abbreviations and acronyms used in the paper are hereinafter listed. Each acronym is however properly introduced when first used in the text.

HAP – Hydroxyapatite; CCU – Carbon Capture and Utilization; FE – Faradaic efficiency; GDE – Gas Diffusion Electrode; 3D-GNS – 3D assembly of Graphene NanoSheets; PEIS – Potentiostatic Electrochemical Impedance Spectroscopy; LSV – Linear Sweep Voltammetry; CA – Chronoamperometry; PBS – Phosphate Buffer Solution.

Acknowledgements

The authors kindly acknowledge the help of Dr. Yuanchao Liu in performing and interpreting N_2 adsorption/desorption isotherms of the samples and the Irvine Materials Research Institute (IMRI) for the access to their facilities.

Supporting information available

Experimental methods, additional characterization and electrochemical data (Figures S1 to S14), and Table S1 and S3.

Author information

Corresponding author
Plamen Atanassov – University of California Irvine, Department of Chemical and Biomolecular Engineering, Irvine, USA; e-mail: plamen.atanassov@uci.edu

Authors
Michele Ferri – Università degli Studi di Milano, Dipartimento di Chimica, Via Golgi 19, Milan, Italy; email: michele.ferri@unimi.it
Laurent Delafontaine – University of California Irvine, Department of Chemical and Biomolecular Engineering, Irvine, USA; email: ldelafon@uci.edu
Shengyuan Guo – University of California Irvine, Department of Chemical and Biomolecular Engineering, Irvine, USA; email: shengyg4@uci.edu
Tristan Asset – University of California Irvine, Department of Chemical and Biomolecular Engineering, Irvine, USA; email: tasset@uci.edu
Pierangela Cristiani – RSE, Ricerca sul Sistema Energetico, Milan, Italy; email: pierangela.cristiani@rse-web.it
Sebastiano Campisi – Università degli Studi di Milano, Dipartimento di Chimica, Via Golgi 19, Milan, Italy; email: sebastiano.campisi@unimi.it
Antonella Gervasini – Università degli Studi di Milano, Dipartimento di Chimica, Via Golgi 19, Milan, Italy; email: antonella.gervasini@unimi.it

Notes

The authors declare no conflict of interest.

References

(1) CO2 Earth - Number for living on Earth https://www.co2.earth/daily-co2.

(2) Qiao, J.; Liu, Y.; Zhang, J. *Electrochemical Reduction of Carbon Dioxide*; Qiao, J., Liu, Y., Zhang, J., Eds.; CRC Press, 2016. https://doi.org/10.1201/b20177.

(3) Kibria, M. G.; Edwards, J. P.; Gabardo, C. M.; Dinh, C. T.; Seifitokaldani, A.; Sinton, D.; Sargent, E. H. Electrochemical CO2 Reduction into Chemical Feedstocks: From Mechanistic Electrocatalysis Models to System Design. *Adv. Mater.* **2019**, *31* (31), 1–24. https://doi.org/10.1002/adma.201807166.

(4) Hori, Y.; Murata, A.; Takahashi, R. Formation of Hydrocarbons in the Electrochemical Reduction

of Carbon Dioxide at a Copper Electrode in Aqueous Solution. *J. Chem. Soc. Faraday Trans. 1 Phys. Chem. Condens. Phases* **1989**, *85* (8), 2309–2326. https://doi.org/10.1039/F19898502309.

(5) Sánchez, O. G.; Birdja, Y. Y.; Bulut, M.; Vaes, J.; Breugelmans, T.; Pant, D. Recent Advances in Industrial CO 2 Electroreduction. *Curr. Opin. Green Sustain. Chem.* **2019**, *16*, 47–56. https://doi.org/10.1016/j.cogsc.2019.01.005.

(6) Nguyen, T. N.; Dinh, C. T. Gas Diffusion Electrode Design for Electrochemical Carbon Dioxide Reduction. *Chem. Soc. Rev.* **2020**, *49* (21), 7488–7504. https://doi.org/10.1039/d0cs00230e.

(7) Liu, K.; Smith, W. A.; Burdyny, T. Introductory Guide to Assembling and Operating Gas Diffusion Electrodes for Electrochemical CO 2 Reduction. *ACS Energy Lett.* **2019**, *4* (3), 639–643. https://doi.org/10.1021/acsenergylett.9b00137.

(8) Endrődi, B.; Bencsik, G.; Darvas, F.; Jones, R.; Rajeshwar, K.; Janáky, C. Continuous-Flow Electroreduction of Carbon Dioxide. *Prog. Energy Combust. Sci.* **2017**, *62*, 133–154. https://doi.org/10.1016/j.pecs.2017.05.005.

(9) Nitopi, S.; Bertheussen, E.; Scott, S. B.; Liu, X.; Engstfeld, A. K.; Horch, S.; Seger, B.; Stephens, I. E. L.; Chan, K.; Hahn, C.; Nørskov, J. K.; Jaramillo, T. F.; Chorkendorff, I. Progress and Perspectives of Electrochemical CO2 Reduction on Copper in Aqueous Electrolyte. *Chem. Rev.* **2019**, *119* (12), 7610–7672. https://doi.org/10.1021/acs.chemrev.8b00705.

(10) Peterson, A. A.; Nørskov, J. K. Activity Descriptors for CO 2 Electroreduction to Methane on Transition-Metal Catalysts. *J. Phys. Chem. Lett.* **2012**, *3* (2), 251–258. https://doi.org/10.1021/jz201461p.

(11) Reske, R.; Mistry, H.; Behafarid, F.; Roldan Cuenya, B.; Strasser, P. Particle Size Effects in the Catalytic Electroreduction of CO2 on Cu Nanoparticles. *J. Am. Chem. Soc.* **2014**, *136* (19), 6978–6986. https://doi.org/10.1021/ja500328k.

(12) Loiudice, A.; Lobaccaro, P.; Kamali, E. A.; Thao, T.; Huang, B. H.; Ager, J. W.; Buonsanti, R. Tailoring Copper Nanocrystals towards C2 Products in Electrochemical CO2 Reduction. *Angew. Chemie - Int. Ed.* **2016**, *55* (19), 5789–5792. https://doi.org/10.1002/anie.201601582.

(13) Mistry, H.; Varela, A. S.; Bonifacio, C. S.; Zegkinoglou, I.; Sinev, I.; Choi, Y. W.; Kisslinger, K.; Stach, E. A.; Yang, J. C.; Strasser, P.; Cuenya, B. R. Highly Selective Plasma-Activated Copper Catalysts for Carbon Dioxide Reduction to Ethylene. *Nat. Commun.* **2016**, *7*. https://doi.org/10.1038/ncomms12123.

(14) Baturina, O. A.; Lu, Q.; Padilla, M. A.; Xin, L.; Li, W.; Serov, A.; Artyushkova, K.; Atanassov, P.; Xu, F.; Epshteyn, A.; Brintlinger, T.; Schuette, M.; Collins, G. E. CO2 Electroreduction to Hydrocarbons on Carbon-Supported Cu Nanoparticles. *ACS Catal.* **2014**, *4* (10), 3682–3695. https://doi.org/10.1021/cs500537y.

(15) Li, Q.; Zhu, W.; Fu, J.; Zhang, H.; Wu, G.; Sun, S. Controlled Assembly of Cu Nanoparticles on Pyridinic-N Rich Graphene for Electrochemical Reduction of CO2 to Ethylene. *Nano Energy* **2016**, *24*, 1–9. https://doi.org/10.1016/j.nanoen.2016.03.024.

(16) Song, Y.; Peng, R.; Hensley, D. K.; Bonnesen, P. V.; Liang, L.; Wu, Z.; Meyer, H. M.; Chi, M.; Ma, C.; Sumpter, B. G.; Rondinone, A. J. High-Selectivity Electrochemical Conversion of CO2 to Ethanol Using a Copper Nanoparticle/N-Doped Graphene Electrode. *ChemistrySelect* **2016**, *1* (19), 6055–6061. https://doi.org/10.1002/slct.201601169.

(17) Zhao, J.; Sun, L.; Canepa, S.; Sun, H.; Yesibolati, M. N.; Sherburne, M.; Xu, R.; Sritharan, T.; Loo, J. S. C.; Ager, J. W.; Barber, J.; Mølhave, K.; Xu, Z. J. Phosphate Tuned Copper Electrodeposition and Promoted Formic Acid Selectivity for Carbon Dioxide Reduction. *J. Mater. Chem. A* **2017**, *5* (23), 11905–11916. https://doi.org/10.1039/c7ta01871a.

(18) Recillas, S.; Rodríguez-Lugo, V.; Montero, M. L.; Viquez-Cano, S.; Hernandez, L.; Castaño, V. M. Studies on the Precipitation Behavior of Calcium Phosphate Solutions. *J. Ceram. Process. Res.* **2012**, *13* (1), 5–10.

(19) Ferri, M.; Campisi, S.; Scavini, M.; Evangelisti, C.; Carniti, P.; Gervasini, A. In-Depth Study of the Mechanism of Heavy Metal Trapping on the Surface of Hydroxyapatite. *Appl. Surf. Sci.* **2019**, *475* (October 2018), 397–409. https://doi.org/10.1016/j.apsusc.2018.12.264.

(20) Diallo-Garcia, S.; Osman, M. Ben; Krafft, J. M.; Casale, S.; Thomas, C.; Kubo, J.; Costentin, G. Identification of Surface Basic Sites and Acid-Base Pairs of Hydroxyapatite. *J. Phys. Chem. C* **2014**, *118* (24), 12744–12757. https://doi.org/10.1021/jp500469x.

(21) Souza, F. S.; Matos, M. J. S.; Galvão, B. R. L.; Arapiraca, A. F. C.; Silva, S. N.; Pinheiro, I. P. Adsorption of CO 2 on Biphasic and Amorphous Calcium Phosphates : An Experimental and Theoretical Analysis. *Chem. Phys. Lett.* **2019**, *714* (August 2018), 143–148. https://doi.org/10.1016/j.cplett.2018.10.080.

(22) Cheng, Z. H.; Yasukawa, A.; Kandori, K.; Ishikawa, T. FTIR Study of Adsorption of CO 2 on Nonstoichiometric Calcium Hydroxyapatite. *Langmuir* **1998**, No. 15, 6681–6686. https://doi.org/10.1021/la980339n.

(23) Wai, M. H.; Ashok, J.; Dewangan, N.; Das, S.; Xi, S.; Borgna, A.; Kawi, S. Influence of Surface Formate Species on Methane Selectivity for Carbon Dioxide Methanation over Nickel Hydroxyapatite Catalyst. *ChemCatChem* **2020**, *12* (24), 6410–6419. https://doi.org/10.1002/cctc.202001300.

(24) Wang, X.; Feng, X.; Shang, J.; Jin, Y.; Zhang, C. Photocatalytic Reduction of CO2 Using Titanium-Substituted and Fluorine-Doped Titanium-Substituted Hydroxyapatite as Photocatalysts. *Catal. Letters* **2017**, *147* (11), 2706–2713. https://doi.org/10.1007/s10562-017-2175-5.

(25) Chong, R.; Fan, Y.; Du, Y.; Liu, L.; Chang, Z.; Li, D. Hydroxyapatite Decorated TiO2 as Efficient Photocatalyst for Selective Reduction of CO2 with H2O into CH4. *Int. J. Hydrogen Energy* **2018**, *43* (49), 22329–22339. https://doi.org/10.1016/j.ijhydene.2018.10.045.

(26) Serov, A.; Atanassov, P. US Patent N° 9,673.456 B2, 2017.

(27) Serov, A.; Andersen, N. I.; Kabir, S. A.; Roy, A.; Asset, T.; Chatenet, M.; Maillard, F.; Atanassova, P. Palladium Supported on 3D Graphene as an Active Catalyst for Alcohols Electrooxidation. *J. Electrochem. Soc.* **2015**, *162* (12), F1305–F1309. https://doi.org/10.1149/2.0301512jes.

(28) Kabir, S.; Artyushkova, K.; Serov, A.; Atanassov, P. Role of Nitrogen Moieties in N-Doped 3D-Graphene Nanosheets for Oxygen Electroreduction in Acidic and Alkaline Media. *ACS Appl. Mater. Interfaces* **2018**, *10* (14), 11623–11632. https://doi.org/10.1021/acsami.7b18651.

(29) Hori, Y.; Takahashi, R.; Yoshinami, Y.; Murata, A. Electrochemical Reduction of CO at a Copper Electrode. *J. Phys. Chem. B* **1997**, *101* (36), 7075–7081. https://doi.org/10.1021/jp970284i.

(30) Ross, M. B.; De Luna, P.; Li, Y.; Dinh, C. T.; Kim, D.; Yang, P.; Sargent, E. H. Designing Materials for

Electrochemical Carbon Dioxide Recycling. *Nat. Catal.* **2019**, *2* (8), 648–658. https://doi.org/10.1038/s41929-019-0306-7.

(31) Wang, H.; Jia, J.; Song, P.; Wang, Q.; Li, D.; Min, S.; Qian, C.; Wang, L.; Li, Y. F.; Ma, C.; Wu, T.; Yuan, J.; Antonietti, M.; Ozin, G. A. Efficient Electrocatalytic Reduction of CO2 by Nitrogen-Doped Nanoporous Carbon/Carbon Nanotube Membranes: A Step Towards the Electrochemical CO2 Refinery. *Angew. Chemie - Int. Ed.* **2017**, *56* (27), 7847–7852. https://doi.org/10.1002/anie.201703720.

FIGURES & TABLES

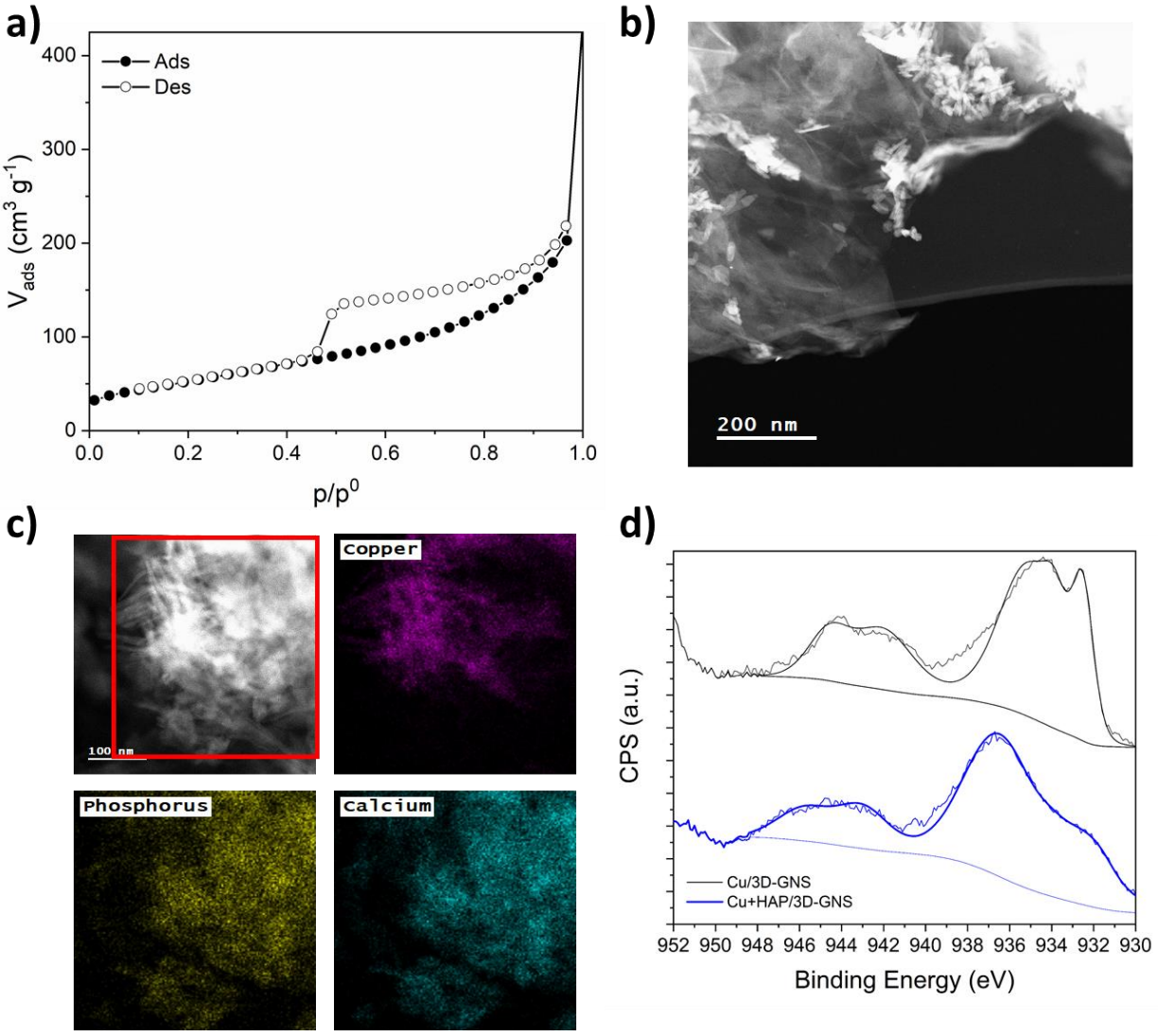

Figure 1: Cu+HAP/3D-GNS characterization: N2 adsorption/desorption isotherm (a), STEM images (b) with correlated STEM/EDX elemental maps (c) and high resolution XPS spectra of the Cu 2p region (d).

Table 1: Structural/morphological and surface compositional features obtained by means of N_2 ads/des and XPS on the pristine 3D-GNS support and both catalysts.

Sample	SA[a]	V_{Pore}[b]	Elemental composition (*at.%*)					
	$m^2\ g^{-1}$	$cm^3\ g^{-1}$	C 1s	O 1s	N 1s	Cu 2p	Ca 2p	P 2s[c]
3D-GNS	209.17	0.214	95.97	2.98	1.25	-	-	-
Cu/3D-GNS	168.88	0.188	92.71	5.81	1.21	0.27	-	-
Cu+HAP/3D-GNS	190.74	0.187	75.20	13.52	0.57	0.27	6.46	3.99

[a] Calculated by linear (2-parameters) BET equation;

[b] PSD calculated according to N_2 – DFT Model

[c] P quantification was performed on P 2s peak and not on P 2p one as to avoid integration errors caused by the overlapping of P 2p and Cu 3s contributions.

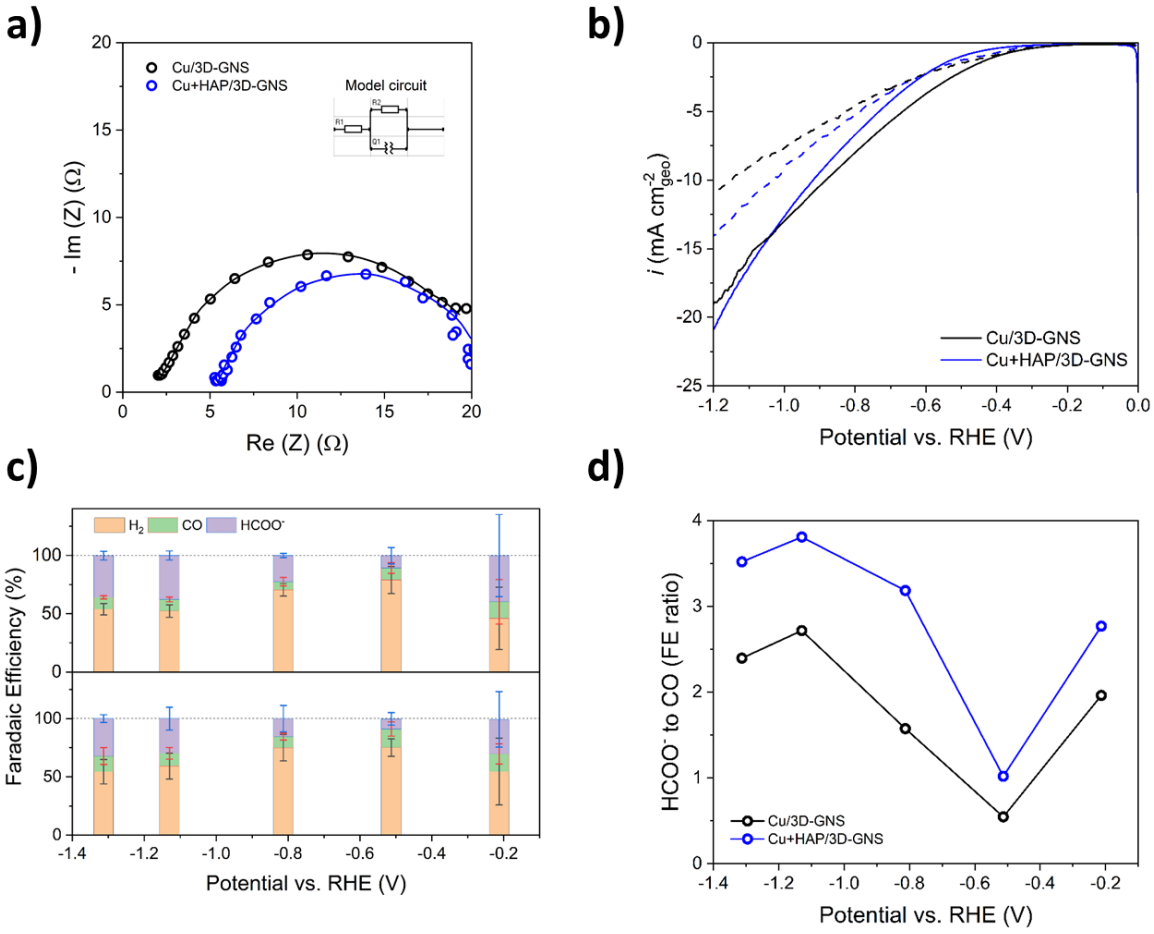

Figure 2: Nyquist plots (a), linear scan voltammetries (b), faradaic efficiencies (bottom: Cu/3D-GNS; top: Cu+HAP/3D-GNS) (c) and formate to CO faradaic efficiency ratio (d) of Cu/3D-GNS and Cu+HAP/3D-GNS catalysts.

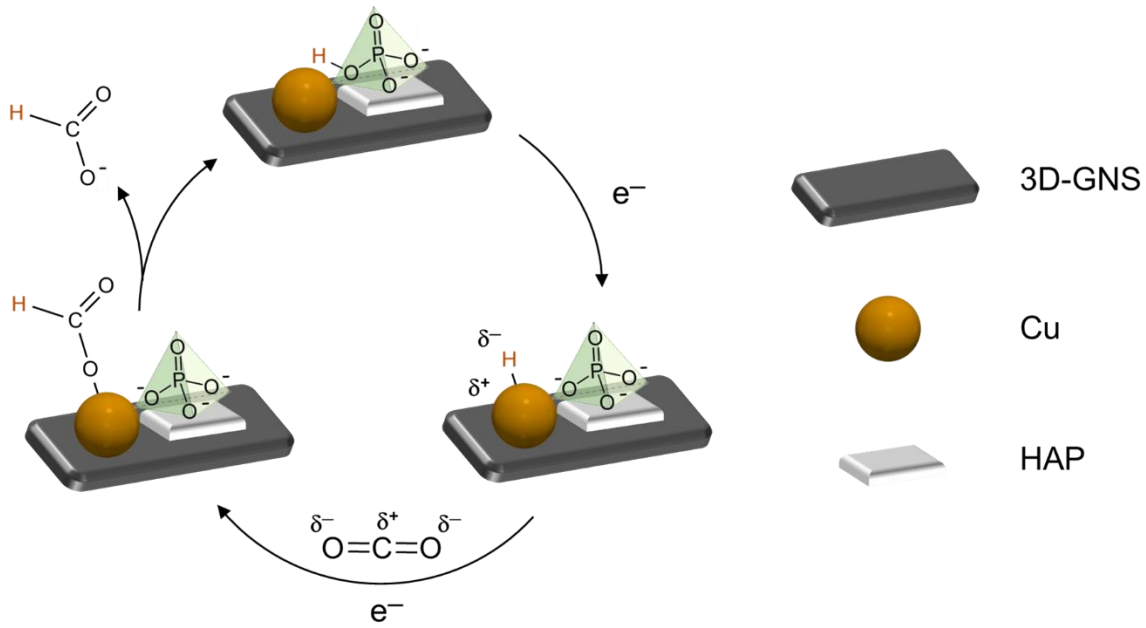

Figure 3: Proposed mechanism for $HCOO^-$ boosted production on the HAP-admixed catalyst